LANGMUIR Article
Cite This: Langmuir 2018, 34, 1645−1654
pubs.acs.org/Langmuir

Hierarchical Surface Patterns upon Evaporation of a ZnO Nanofluid Droplet: Effect of Particle Morphology

Patryk Wąsik,[†,§] Christian Redeker,[§] Thomas G. Dane,[∥] Annela M. Seddon,[†,‡] Hua Wu,[§] and Wuge H. Briscoe*[,§]

[†]Bristol Centre for Functional Nanomaterials (BCFN), HH Wills Physics Laboratory, and [‡]School of Physics, HH Wills Physics Laboratory, University of Bristol, Tyndall Avenue, Bristol BS8 1TL, U.K.

[§]School of Chemistry, University of Bristol, Cantock's Close, Bristol BS8 1TS, U.K.

[∥]The European Synchrotron (ESRF) 71, Avenue des Martyrs, Grenoble, France

Supporting Information

ABSTRACT: Surface structures with tailored morphologies can be readily delivered by the evaporation-induced self-assembly process. It has been recently demonstrated that ZnO nanorods could undergo rapid chemical and morphological transformation into 3D complex structures of $Zn(OH)_2$ nanofibers as a droplet of ZnO nanofluid dries on the substrate via a mechanism very different from that observed in the coffee ring effect. Here, we have investigated how the crystallinity and morphology of ZnO nanoparticles would affect the ultimate pattern formation. Three ZnO particles differing in size and shape were used, and their crystal structures were characterized by powder X-ray diffraction (XRD) and transmission electron microscopy (TEM). Their dispersions were prepared by sonication in a mixture of isobutylamine and cyclohexane. Residual surface patterns were created by drop casting a droplet of the nanofluid on a silicon substrate. The residual surface patterns were analyzed by scanning electron microscopy (SEM) and microfocus grazing incidence X-ray diffraction (μGIXRD). Nanofluid droplets of the in-house synthesized ZnO nanoparticles resulted in residual surface patterns consisting of $Zn(OH)_2$ nanofibers. However, when commercially acquired ZnO powders composed of crystals with various shapes and sizes were used as the starting material, $Zn(OH)_2$ fibers were found covered by ZnO crystal residues that did not fully undergo the dissolution and recrystallization process during evaporation. The difference in the solubility of ZnO nanoparticles was linked to the difference in their crystallinity, as assessed using the Scherrer equation analysis of their XRD Bragg peaks. Our results show that the morphology of the ultimate residual pattern from evaporation of ZnO nanofluids can be controlled by varying the crystallinity of the starting ZnO nanoparticles which affects the nanoparticle dissolution process during evaporation.

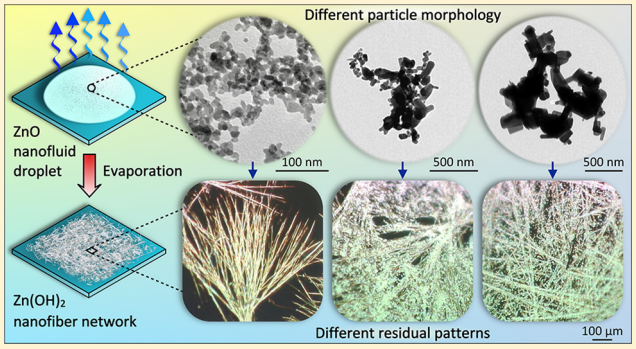

INTRODUCTION

Controlled assembly at interfaces on a nanoscale is central in nanoscience and important to application of nanomaterials,[1,2] and considerable effort has been devoted to creating patterned surfaces with tailored structures and enhanced functionalities. A simple and versatile bottom-up approach for generating surface patterns is evaporation induced self-assembly (EISA).[3] In this process, particles (nanoparticles, polymers, biomaterials, etc.) dispersed in a drying droplet are arranged into a variety of structures as the result of the delicate, temporally and spatially fluctuating balance between interparticle forces[4,5] and evaporation-induced solvent flows. This balance may be tuned by manipulating parameters such particle size, shape, concentration, solvent composition, evaporation rate, and surface chemistry of the substrate. EISA has been successfully applied to applications such as inject printing of carbon nanotubes,[6] production of conductive graphene networks,[7] transparent films,[8] DNA microarrays,[9] ultraviolet photodetectors,[10] mesoporous carbons,[11] photoluminescent films,[12] bacterial deposits,[13] and evaporative cooling.[14]

The most commonly observed deposition patterns resulting from the EISA process are so-called "coffee rings".[15−17] When the contact line between the droplet and the substrate is pinned upon evaporation, an outward capillary flow of liquid is induced to compensate faster liquid loss at the droplet edge. This carries the dispersed solutes to the droplet perimeter, where they are deposited and form the ringlike residual pattern.

The formation of coffee rings can be suppressed by the inward Marangoni flow that carries particles toward the droplet center[18] or by the shape anisotropy of dispersed particles.[19]

Received: November 8, 2017
Revised: December 23, 2017
Published: January 2, 2018

DOI: 10.1021/acs.langmuir.7b03854
Langmuir 2018, 34, 1645−1654

The residual EISA pattern may also be affected by convective instabilities in the drop,[20] which manifest as multiple vortices with liquid flowing upward in the center and subsequently outward to the edge of the convection cell, such as the Bénard–Marangoni and the Rayleigh–Bénard convection,[21] which could lead to residual patterns of connected polygons templating the convective cells.

Fingering structures may also form from EISA due to fluctuations at the interface between two fluids of different viscosities.[22−24] Fingerlike stripes perpendicular to the contact line are often produced in vertical deposition techniques (i.e. plate withdrawal), and radial spoke patterns are commonly observed in horizontal deposition techniques (i.e., drop casting).[25]

Very recently, we have made an unexpected observation of residual surface patterns from an EISA process.[26] When a tiny droplet of a nanofluid containing ZnO nanorods dries on a glass slide at room temperature, a uniform thin film with a 3D porous network structure comprising centimeter long $Zn(OH)_2$ nanofibers and dendrites can spontaneously form. The observation of this rapid chemical (ZnO to $Zn(OH)_2$) and morphological (nanorods to centimeter long fibers) transformation of a drying nanofluid is surprising and reveals a new mechanism, which is very different from that associated with the coffee rings, as outlined below. Once a droplet containing ZnO nanorods in an isobutylamine and cyclohexane mixture is placed on the substrate surface, water molecules present in air are taken up by the solvent due to the high miscibility of isobutylamine with water. These water molecules are then incorporated to the surface of isobutylamine-coated ZnO nanorods, where isobutylamine undergoes hydrolysis with entrained water molecules, raising pH within the proximity of ZnO nanorods. When pH reaches a value above 9, ZnO nanorods transform into soluble hydroxyl complexes with ZnOH coordinated with isobutylamine. Those complexes may further assemble in clusters that serve as building blocks in the formation of zinc hydroxide nanocrystals, whose self-organization is driven by the thermal and solutal Marangoni flows and instabilities during the evaporation. This ultimately leads to the residual surface pattern composed of a uniform film with the structure of 3D fiber networks being formed on a substrate.

A key step involved in this mechanism is initial moisture-assisted rapid dissolution of isobutylamine-coated ZnO nanorods that differs from previous studies where the dispersed particles were typically inert. However, a question concerning this novel EISA process remains: is it necessary to use the ZnO nanoparticles of size and morphology (i.e., nanorods)[26] to produce the hierarchical residual surface patterns? To address this question, in this work we have used three different ZnO particles varying in shape, size, and crystal structure in the nanofluid dispersion for the EISA process and investigated how the initial structure and morphology of ZnO nanocrystals would affect the ultimate residual pattern formation. ZnO particles were dispersed in a mixture of cyclohexane and isobutylamine and dried on a silicon substrate. The starting particles were characterized by X-ray powder diffraction (XRD), transmission electron microscopy (TEM) and energy-dispersive X-ray spectroscopy (EDX), ZnO nano/microfluids by dynamic light scattering (DLS), and the obtained residual surface patterns by scanning electron microscopy (SEM) and microfocus grazing incidence X-ray diffraction (μGIXRD). It was demonstrated that the morphology of the final residual surface pattern from a drying ZnO-nano/microfluid droplet could be controlled by varying the crystallinity of the starting ZnO particles, which affected the initial ZnO dissolution mechanism.

MATERIALS AND METHODS

ZnO Particles. Three types of zinc oxide (ZnO) particles were used: in-house synthesized ZnO nanoparticles and commercially acquired ZnO nanopowder (Sigma-Aldrich, <100 nm particle size, ∼80% Zn basis) and ZnO powder (Sigma-Aldrich, ACS reagent, ≥99.0% (KT)). The in-house ZnO nanoparticles synthesis was carried out according to a modified method described by Sun et al.[27] as detailed in the Supporting Information section SI1.

Particle Characterization. Particles morphology was analyzed by TEM (see section SI2 for details). The sizing of the in-house synthesized ZnO nanoparticles and commercially acquired ZnO nanopowder and ZnO powder was performed using ImageJ software (see section SI3 for details). The structure of ZnO particles was analyzed by XRD (see section SI4 for details) and their chemical composition by EDX (see section SI5).

Substrates. Silicon wafers (ID 452, UniversityWafer, Inc.) were cut into ∼1 × 1 cm^2 squares using a pen diamond cutter. The substrates were then sonicated in acetone and ethanol for 10 min each, then rinsed three times with Milli-Q water, before sonicated in Milli-Q water for 10 min, and dried with a stream of nitrogen.

Evaporative Drying of ZnO Nano/Microfluid Droplets. ZnO particles were dispersed in a mixture of cyclohexane and isobutylamine (5:1 volume:volume ratio), the same solvent composition as in ref 26. (The effect of the solvent composition on the residual pattern will be reported elsewhere.) Suspensions of the final ZnO concentration of 1 mg/mL were sonicated for 2 h to form homogeneous dispersions. As-prepared ZnO nano/microfluids were studies with DLS (see section SI6). 30 μL droplets of ZnO nanofluids were drop-cast by a pipet onto the surface of the substrates placed inside compartments of a polystyrene Petri dish (25 compartment sterile 100 mm box; Sterilin) and left to evaporate. The process took place at room temperature (∼23 °C) and relative humidity (RH) ∼45%, measured with a humidity/temperature pen (Tracable). Within several minutes all droplets evaporated leaving the substrates covered with white deposits.

Characterization of the Residual Surface Patterns Resulted from Evaporative Drying. Residual surface patterns formed by the evaporative drying of ZnO nano/microfluids were investigated using SEM (JSM-IT300 SEM, JEOL), optical microscopy (see section SI7), and microfocus grazing incidence X-ray diffraction (μGIXRD). μGIXRD analysis of the residual surface patterns was performed at Beamline ID13 at the European Synchrotron Radiation Facility (France) (see section SI8 for details).

Crystallinity Assessment of ZnO (Nano)particles. The crystallinity of the ZnO samples was evaluated using the Sherrer formula[30] to yield the coherence length L_a, which gives an indication of the lower limit of the crystal domain size[31,32] (see section SI4 for details).

RESULTS AND DISCUSSION

Characterization of ZnO Nano/Microparticles. TEM micrographs and the corresponding size distributions of ZnO particles are shown in Figure 2. The in-house synthesized ZnO sample was largely composed of spherically shaped nanocrystals (Figure 2a). Their size distribution (Figure 2d) was fitted with the log-normal distribution function (see section SI3) with the geometric mean particle size M = 9.2 nm and the geometric standard deviation σ_g = 1.3.

In contrast, the commercially acquired ZnO particles (Figure 2b,c) exhibited diverse morphologies, including spherical, faceted, elongated rodlike, and irregular parallelepiped structures, with a wide size distribution. Therefore, a maximum dimension parameter, which is the greatest distance between any two surface points of the particle and can be directly

DOI: 10.1021/acs.langmuir.7b03854
Langmuir 2018, 34, 1645−1654

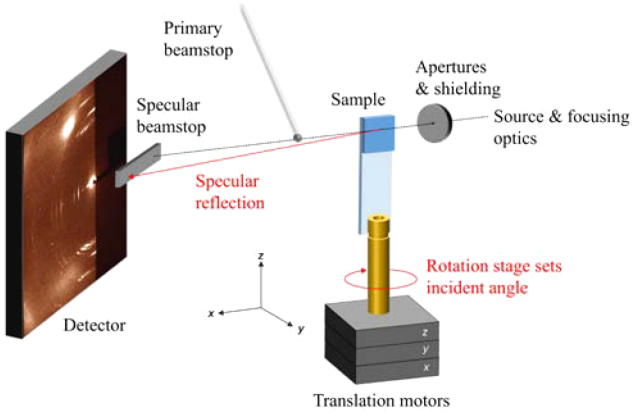

Figure 1. Experimental setup for μGIXRD analysis. A sample with residual surface patterns was glued to a glass slide and mounted on the top of translation/rotation stage. Sample's surface was scanned with X-rays by moving the sample position along z-axis and recording a μGIXD pattern every 2 μm. The "Position" parameter in Figures 7 and 8 refers to the position of the X-ray beam between edges of the sample along the z-axis.

measured in the case of aspherical particles,[37] was used as a variable of a size distribution instead of a diameter for commercially acquired ZnO nanopowder and ZnO powder.

The ZnO nanopowder sample (Figure 2b) had particle sizes varying from 10 nm for the smallest spherical particles to up to 530 nm elongated parallelepiped crystals. The size distribution of the ZnO nanopowder sample is shown in Figure 2e, with calculated log-normal fit parameters of M = 71.7 nm (the mean maximum dimension) and σ_g = 2.0. This means that 68.3% of all particles in ZnO nanopowder sample had the maximum dimension between 36.2 and 141.8 nm (between M/σ_g and $M\sigma_g$). The ZnO powder (Figure 2c) contained particles with sizes ranging from 15 nm for the smallest spheres to more than 1 μm for elongated crystals, with log-normal fit parameters M = 133.4 nm and σ_g = 2.2. On the basis of its size distribution analysis (Figure 2f), it is concluded that 68.3% of all particles in ZnO powder sample exhibited the maximum diameter between 61.2 and 290.9 nm.

Figure 3 presents XRD diffraction profiles of the three types of ZnO particles. All the peaks were characteristic for a wurtzite structure of ZnO (PDF 01-075-0576). The XRD line profile of the in-house synthesized ZnO sample (cf. Figure 2a) exhibits large peak broadening. The line profiles of commercially acquired ZnO particles, nanopowder, and powder (cf. Figure 3b,c) show sharp peaks. The XRD results indicate that the commercial ZnO nanopowder and powder samples possessed higher crystallinity (larger size of coherently scattering domains and less strain caused by crystal defects) compared to the in-house prepared ZnO nanoparticles.

Table 1 lists the calculated coherence lengths according to eq S3, where the value for the shape constant K = 1 was used, and their corresponding errors were calculated by the partial derivative method[31,32] for the six peaks in the XRD line profiles of the in-house synthesized ZnO nanoparticles, ZnO nanopowder, and ZnO powder. Among the three most pronounced peaks, (100), (002), and (101), the coherence length L_a corresponding to the (002) plane diffraction for all samples is the largest, indicating that the crystallites were elongated in the (002) direction (c-axis), which is the preferential ZnO crystal growth direction during synthesis.[38,39] The shortest average

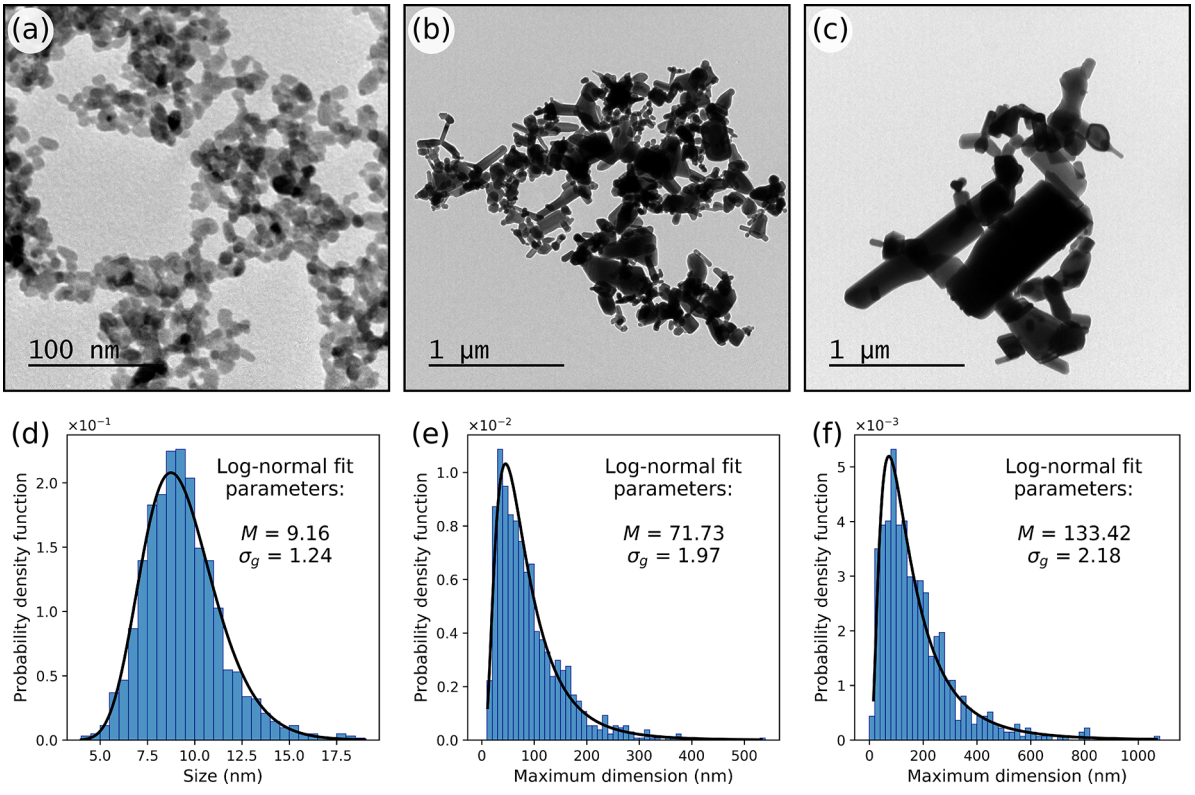

Figure 2. TEM micrographs of the ZnO particles: (a) the in-house synthesized ZnO nanoparticles, and commercially acquired (b) ZnO nanopowder and (c) ZnO powder. Below the micrographs, the corresponding size distributions for particles (d) diameter and (e, f) maximum dimension are shown for (a), (b), and (c), respectively.

DOI: 10.1021/acs.langmuir.7b03854
Langmuir 2018, 34, 1645−1654

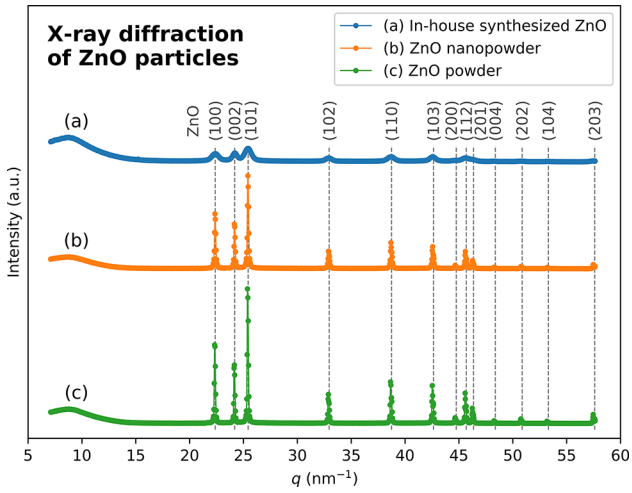

Figure 3. Powder XRD profiles of ZnO particles used for the preparation of nanofluids: (a) in-house synthesized ZnO nanoparticles, (b) ZnO nanopowder (Sigma-Aldrich), and (c) ZnO powder (Sigma-Aldrich). The numbers in parentheses are the Miller indices of the crystallographic planes of ZnO (PDF 01-075-0576).

Table 1. Calculated Correlation Lengths (L_a) and Errors (δL_a) for the Six Most Pronounced Peaks Based on a Gaussian Fit to the Experimental X-ray Diffraction Line Profiles of the In-House Prepared ZnO Nanoparticles and Commercially Acquired ZnO Nanopowder and ZnO Powder

	In-house synthesized ZnO NP		ZnO nanopowder		ZnO powder	
Peak (*hkl*)	L_a (nm)	$\pm\delta L_a$ (nm)	L_a (nm)	$\pm\delta L_a$ (nm)	L_a (nm)	$\pm\delta L_a$ (nm)
(100)	7.6	0.1	44.6	0.6	50.4	0.8
(002)	10.4	0.1	49.8	0.9	51.5	1.1
(101)	8.0	0.1	42.5	0.3	47.6	0.4
(102)	9.3	0.2	38.3	1.6	42.6	1.8
(110)	8.2	0.1	35.9	1.0	38.7	1.1
(103)	10.1	0.2	34.1	1.2	36.8	1.3
Average:	8.9		40.9		44.6	

coherence length, L_a = 8.9 nm, was exhibited by the in-house synthesized ZnO nanoparticles, which is comparable to its geometric median diameter for log-normal distribution, M = 9.2 nm (68.3% of all particles between M/σ_g = 7.4 nm and $M\sigma_g$ = 11.4 nm, cf. section SI3). The intermediate value, L_a = 40.9 nm, was shown by ZnO nanopowder and the largest, L_a = 44.6 nm, by ZnO powder. These values are indicative of the lower limit of the apparent crystallite size, with the shape constant, K, in eq S3 accounting for a distribution of shapes as well as for a distribution of sizes to some degree. Even though the value of 8.9 nm correlates with the geometric median particles diameter in log-normal size distribution obtained from TEM analysis of the in-house prepared ZnO sample (Figure 2a,b), TEM micrographs of the other two samples, nanopowder and powder, show that the crystals present in these sample had dimensions much larger than 100−150 nm, and that is the upper limit of the grain size for which the XRD analysis remains valid.[40] Overall, the TEM analysis shows that the in-house ZnO nanoparticles were smaller, with a narrower size distribution, as compared with the commercially acquired ZnO particles, which appeared polycrystalline with larger particles comprising multiple crystal domains.

In addition, ZnO particles were characterized with EDX (cf. section SI5). The results shown in Figure S1 and Table S2 indicate that small amounts of carbon, likely due to airborne contaminants, were present within all samples (3−6 atomic %). However, as they were dispersed in a mixture of organic solvents and sonicated for 2 h before drop casting, it is conceivable that the trace carbon dissolved and did not significantly influence the EISA process.

Residual Surface Patterns from ZnO Nanofluid Dispersion of Different Particle Size and Morphology. The DLS measurements of the ZnO nano/microfluids immediately after the sonication (see section SI6) indicated cluster formation, with polydisperse clusters of size 1−2 μm in all ZnO nano/microfluids (Table S2), suggesting the suspensions were not inherently stable over time. Evaporation of the droplet occurred on a much shorter time scale, and clustering happened for all the samples to the same extent and thus could not account for the vastly different surface patterns observed.

SEM image of the residual surface patterns from the nanofluid of the in-house ZnO nanoparticles shows densely packed patches (Figure 4a), with a distinct peripheral coffee

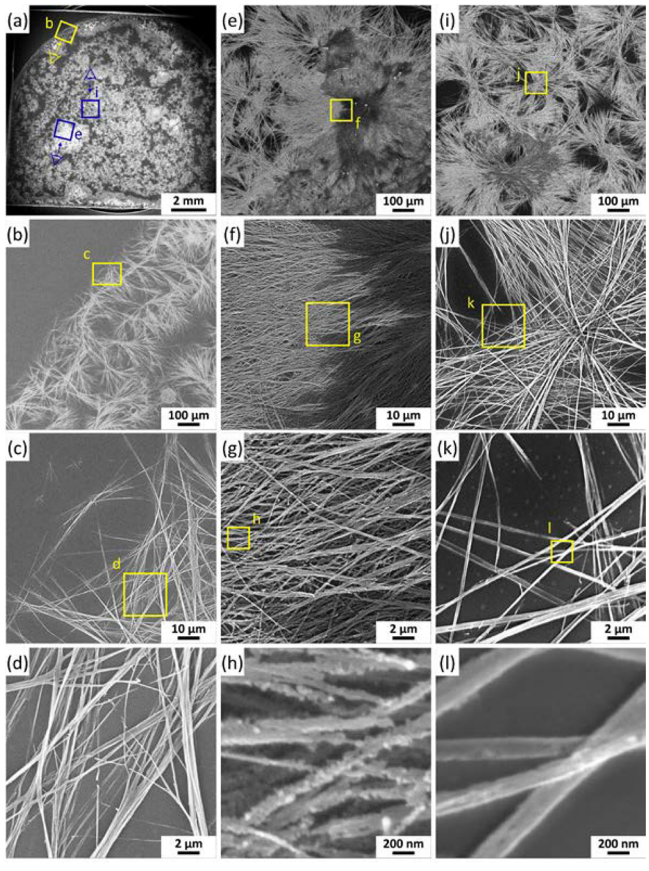

Figure 4. SEM images of the residual surface patterns from evaporative drying of a 30 μL ZnO nanofluid sessile droplet on an ~1 × 1 cm^2 silicon wafer at room temperature and relative humidity of ~45%. The nanofluid was prepared from the in-house synthesized ZnO nanoparticles, dispersed in a mixture of cyclohexane and isobutylamine (5:1 volume:volume ratio). The rectangular regions in the figures are enlarged, with their labels corresponding to those of the figures. The schematic drawings of the eye and arrow in (a) indicate the direction of viewing of the regions as shown in their corresponding magnified images.

DOI: 10.1021/acs.langmuir.7b03854
Langmuir 2018, 34, 1645−1654

ring (Figure 4b). These patches, approximately circular in shape and 475 μm on average in diameter, resemble spokelike radial patterns, with some of them exhibiting a bow-tie projection. Most of them have a center from which the fibers radiate. These structures appear mostly as well-defined cells, overlapping or interpenetrating with each other (Figure 4i) at the edges. There are however some regions of high density with a large degree of overlapping (Figure 4e). The main difference between these regions is the presence of small, irregular residues covering the surface of the fibers located in the high-density regions (Figure 4h), which are not present in the low-density regions (Figure 4d,l).

Figure 5 shows an optical photograph and SEM images of the residual surface patterns from ZnO nanopowder (cf. Figure 2c) nanofluid on a silicon substrate. The entire surface is covered by a dense, fibrous network composed of structures resembling the spokelike radial patterns of a bow-tie projection. The network has the highest density in the central region of the surface (Figure 5b), and is less dense, with small particulate residues between fibrous "bow ties", closer to the perimeter (Figure 5c). The higher magnification images (Figure 5d,g) show that the fibers are covered with particulate residues and aggregates, especially where fibers intersect (Figure 5e,h). The structure of these aggregates (Figure 5f,i) is similar to that of the ZnO nanopowder crystals originally used (Figure 2b).

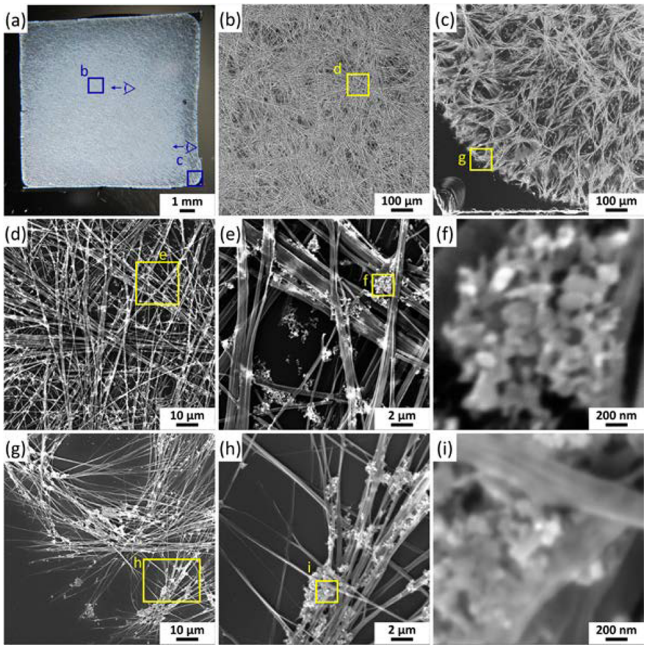

Figure 5. Optical (a) and SEM (b–i) images of the residual surface patterns from evaporative drying of 30 μL of ZnO nanofluid sessile droplet on an ~1 × 1 cm^2 silicon wafer at room temperature and relative humidity (RH) ~ 45%. The nanofluid was prepared from the commercially acquired ZnO nanopowder and dispersed in a mixture of cyclohexane and isobutylamine (5:1 volume:volume ratio). The rectangular regions in the figures are enlarged, with their labels corresponding to those of the figures. The schematic drawings of the eye and arrow in (a) indicate the direction of viewing of the regions as shown in their corresponding magnified images.

In Figure 6, the optical and SEM images of the residual surface patterns from evaporative drying of ZnO nanofluid containing the commercially acquired ZnO powder (cf. Figure 2c) are presented. Similar to the patterns from the ZnO nanopowder nanofluid (Figure 5), the entire surface is covered by a dense, fibrous structure. The structures in the central part of the surface (Figure 6b) have the appearance of the spokelike radial patterns of a bow-tie projection, with the dendritic fibers radiating from the center. At the edge of the substrate (Figure 6c), elongated dendritic fibers extend in a direction perpendicular to the edge forming branched structures pointing inward. Higher magnification images of both central and peripheral areas (Figure 6d–i) show that the constituent fibers are decorated with a large number of aggregates, distributed along the fibrous framework, also in areas where fibers do not cover the substrate. A magnified image of one of these aggregates (Figure 6f) indicates that it was formed from crystals exhibiting very similar structures and dimensions to those of the ZnO powder (cf. Figure 2c) used to prepare the ZnO dispersion.

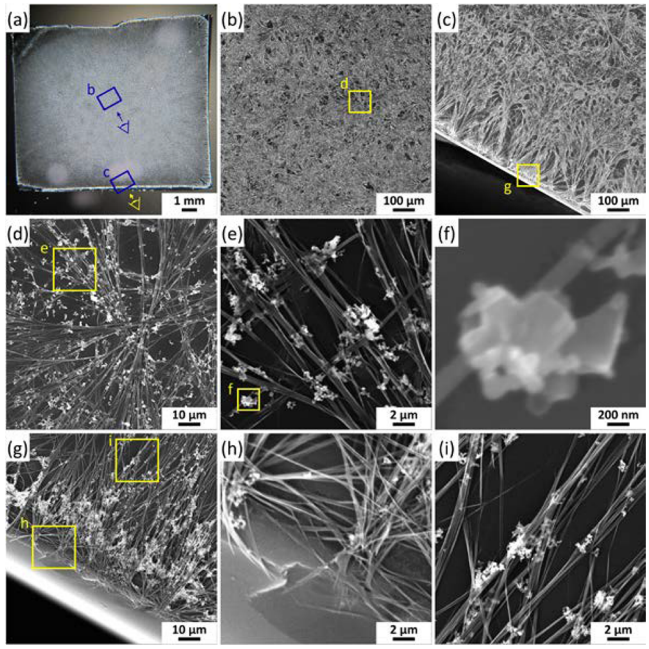

Figure 6. Optical (a) and SEM (b–i) images of the residual surface patterns from evaporative drying of a 30 μL of ZnO nanofluid sessile droplet on an ~1 × 1 cm^2 silicon wafer at room temperature and relative humidity of ~45%. The nanofluid was prepared from the commercially acquired ZnO powder, dispersed in a mixture of cyclohexane and isobutylamine (5:1 volume:volume ratio). The rectangular regions in the figures are enlarged, with their labels corresponding to those of the figures. The schematic drawings of the eye and arrow in (a) indicate the direction of viewing of the regions as shown in their corresponding magnified images.

All three types of dispersions produced residual surface patterns composed of fibrous 3D networks, and the main difference is the amount of the small aggregates incorporated into the fibrous matrix. All the surfaces were covered by similar structures of the spokelike radial patterns, but the coverage and overlapping of these structures were the highest for the patterns produced from the commercially acquired ZnO nanopowder and powder. Additional optical microscopy images can be seen in Figure S2.

The crystal structure of the residual surface patterns formed upon evaporation of ZnO (nano)fluids on a silicon wafer was studied by μGIXRD. Figures 7 and 8 present 2D heat maps (intensity vs momentum transfer vector q) from the μGIXRD data by recording an X-ray diffraction pattern at every 2 μm

DOI: 10.1021/acs.langmuir.7b03854
Langmuir 2018, 34, 1645–1654

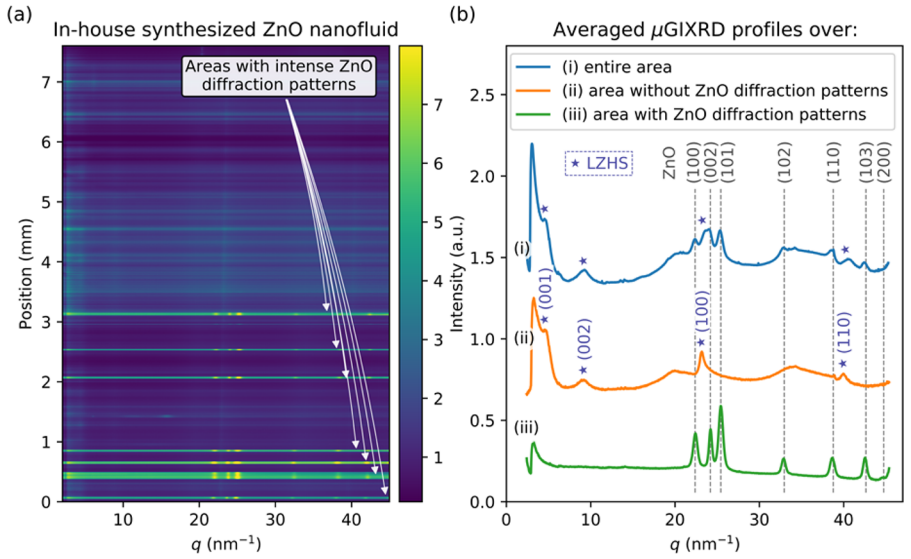

Figure 7. μGIXRD analysis of the residual surface patterns from evaporative drying of a 30 μL ZnO nanofluid sessile droplet on an ∼1 × 1 cm^2 silicon wafer at room temperature and relative humidity of ∼45%. The nanofluid was prepared from the in-house synthesized ZnO nanoparticles, dispersed in a mixture of cyclohexane and isobutylamine (5:1 volume:volume ratio). (a) shows a 2D intensity heat map with respect to position of the scan point on the sample (along *z*-axis in Figure 1) and momentum transfer vector, *q*. Arrows show regions of the sample that produced intense ZnO diffraction patterns. Intensity (a.u.) shown in (a) was calculated as a percentile in the range 0.05−99.95% for better contrast. (b) μGIXRD line profiles averaged over (i) the entire scan area, (ii) the area that did not show ZnO diffraction patters, and (iii) the area with intense ZnO diffraction patterns, marked with arrows in (a). ZnO peaks are indexed in accordance with the reference pattern (PDF 01-075-0576), and layered zinc hydroxide (LZH) structures are labeled with star markers "★" and indexed according to refs 44 and 45.

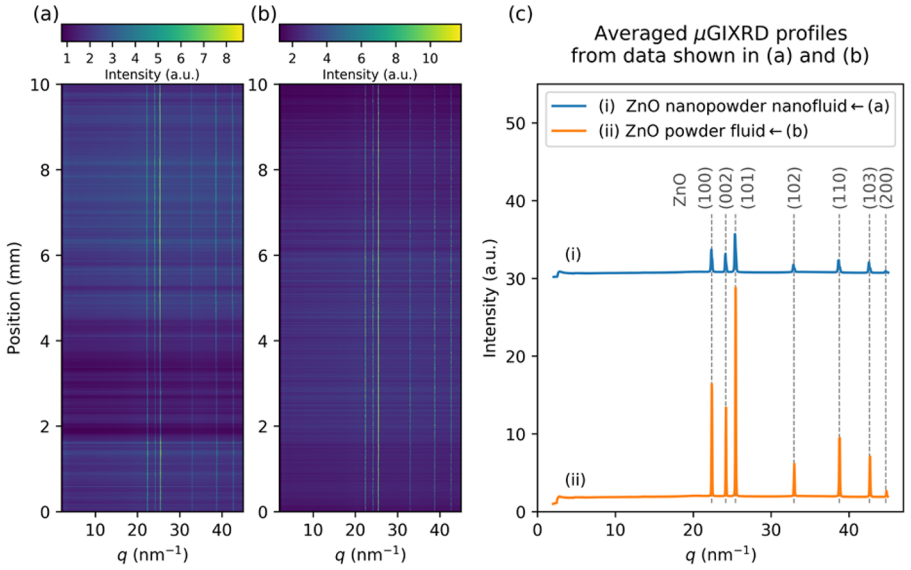

Figure 8. μGIXRD analysis of the residual surface patterns from evaporative drying of a 30 μL ZnO (nano)fluid sessile droplets on a ∼ 1 × 1 cm^2 silicon wafer at room temperature and relative humidity of ∼45%. The (nano)fluids were prepared from comercially acquired ZnO nanopowder and ZnO powder, dispersed in a mixture of cyclohexane and isobutylamine (5:1 volume:volume ratio). (a) and (b) show 2D intensity heat maps for surface patterns from ZnO nanopowder and ZnO powder (nano)fluids, respectively. These heat maps are plotted with respect to position of the scan point on the sample (along the *z*-axis in Figure 1) and momentum transfer vector, *q*. Intensities (a.u.) in (a) and (b) were calculated as a percentile in the range 0.1−99.9% and 0.3−99.7%, respectively, to improve the contrast. (c) μGIXRD line profiles averaged over the entire scan areas for (i) patterns from ZnO nanopowder nanofluid (data in (a)) and (ii) patterns from ZnO powder fluid (data in (b)).

interval across the *z*-axis (Figure 1). To provide statistical information for each sample, diffraction profiles were averaged across the scan area of interest and are shown as line plots in Figures 7b and 8c.

The μGIXRD profile of the residual surface patterns produced from the in-house synthesized ZnO nanoparticles (Figure 7a) exhibits strong diffraction peaks (arrows in Figure 7a) which account for ∼5% of the total area. These diffraction peaks can be assigned to ZnO according to the ZnO reference standard (PDF 01-075-0576), with the corresponding line profile shown in Figure 7b (line iii). The line profile averaged over the remaining 95% of the scanned area is presented as line ii in Figure 7b, showing no ZnO diffractions. All the peaks attributed to the layered zinc hydroxide (LZH) structures are marked with "★" (star) on line profiles i and ii in Figure 7b. For instance, the two peaks in the low *q* range correspond to

DOI: 10.1021/acs.langmuir.7b03854
Langmuir 2018, 34, 1645−1654

the interplanar spacing d = 1.37 nm (q = 4.60 nm^{-1}) and d = 0.68 nm (q = 9.20 nm^{-1}) and can be indexed as (001) and (002) LZH planes and interlayer anionic species complex structures.[42,43] The peaks at d = 0.27 nm (q = 23.17 nm^{-1}) and 0.52 nm (q = 39.99 nm^{-1}) are indexed as (100) and (110), respectively of the brucite-type zinc hydroxide structure.[44,45]

The 2D intensity heat maps (Figure 8a,b) from the μGIXRD profiles of ZnO nanopowder and ZnO powder samples exhibit intense ZnO diffraction patterns throughout the entire scanned area, also evident from the corresponding line profiles in Figure 8c. However, no LZH diffractions are observed. This suggests that the main crystalline phase present is zinc oxide, consistent the SEM images (Figures 5 and 6) that revealed the abundance of ZnO crystals covering the fibrous network in all the areas.

The distribution of the ZnO phase within the residual surface patterns differs among the three types of ZnO nano/microfluids investigated. Zinc oxide diffraction patterns are present only in about 5% of the scanned area in the case of in-house synthesized ZnO nanofluid, while they are manifested uniformly throughout μGIXRD profiles with much higher intensities for the other two nano/microfluids.

The crystallinity of the residual ZnO (nano)crystal aggregates present within residual surface patterns was further evaluated from the peak broadening in the line profiles (Figures 7b and 8b). The coherence length L_a values are listed in Table S4 and discussed in some detail in the Supporting Information (cf. section SI9). In general, the L_a values for the ZnO residual nano(crystals) follow the same trend as the starting particles used for the preparation of ZnO nanofluids.

FURTHER DISCUSSION ON THE EFFECT OF PARTICLE MORPHOLOGY

The particles in the commercially acquired ZnO nanopowder and powder showed a wide range of morphologies and particle size distribution. These anisotropic particles could have affected capillary interactions in a drying droplet by forming loosely packed, quasi-static, or arrested structures at the droplet surface.[19] As the mobility of these particles was reduced, they could have restrained the outward capillary flow in induced by evaporation Bénard cells, contrary to in-house synthesized sample with a more monodisperse shape and size distribution, which produced well-specified spokelike radial patterns of a bow-tie projection on the surface.

It has been previously observed that when ZnO nanofluids were dried at relative humidity ~30%, ZnO nanorods and their large aggregates coexisted with short zinc hydroxide fibers, as the ambient H_2O molecules were crucial for the moisture assisted dissolution of ZnO nanorods.[26] Our experiments were performed at RH about 45%, which explains the presence of undissolved ZnO nanoparticles due to insufficient water molecule uptake from ambient air during droplet drying.

Residual surface patterns produced from the commercially acquired ZnO nanopowder and ZnO powder samples exhibited intense ZnO wurtzite diffraction peaks across all the μGIXRD scanned regions (Figure 8) due to the more prominent presence of undissolved ZnO residues. This is consistent with the SEM observations which confirmed that a network of residual fibers was covered by a large number of crystal agglomerates, accumulating especially at the fiber intersections (Figures 5 and 6). These agglomerates are attributed to ZnO crystals that did not undergo the complete dissolution−recrystallization process, which is a key step in the formation of hierarchical surface morphologies in the novel EISA process.[26]

The coherence length, L_a, from the line profile analysis of μGIXRD peaks of the undissolved ZnO particles in the residual patterns was larger than that from the XRD peak analysis for the starting particles for all the three samples (cf. Table 1 and Table S4) The relative change in the correlation length varies on the type of ZnO compound used and amounts to 19.5%, 20.0%, and 35.3% for the in-house synthesized ZnO and commercially acquired ZnO nanopowder and powder, respectively. This suggests that less crystalline particles underwent dissolution preferentially, whereas the more crystallinity particles remained. Upon evaporation, these particles aggregated, forming agglomerates which were deposited across the fibrous network of the residual patterns.

Dissolution of the nanoparticles has been previously considered in terms of the Ostwald−Freundlich (i.e., the modified Kelvin) equation, particularly within pharmaceutical nanotechnology (cf. section SI10).[46] Accordingly, this equation predicts that the solubility will increase exponentially with decreasing particle size. David et al.[47] studied the solubility of ZnO nanoparticles of three different average particle diameters of 6, 20, and 71 nm and found that the particles larger than 20 nm had the same solubility as that of the bulk material, whereas the 6 nm particles exhibited the highest solubility, as predicted by the Ostwald−Freundlich equation. Mudunkotuwa et al.[48] found that smaller ZnO nanoparticles (4−7 nm) showed a greater extent of dissolution compared to larger particles; however, the solubility of larger particles (15−130 nm) did not differ significantly.

Shape-dependent surface enthalpy at the nanoscale level has also been discussed in terms of exposed surface structures. Crystal surfaces are complex and may exhibit a variety of planes, kinks, steps, and defect sites, which lead to a different bonding environment compared to the bulk. The distribution of these structures can vary between particles and is often dependent on sample preparation. Meulenkamp[49] observed size-dependent chemical reactivity in ZnO nanoparticles (of size 7.0−2.5 nm), which was attributed to the variations in the defect density and surface faceting of the nanocrystals. Gerischer and Sorg[50] showed that the dissolution rate of single crystal ZnO hexagonal needles was dependent on the crystal surface orientation. Michaelis et al.[51] showed that the dissolution behavior of polar and nonpolar crystal surfaces of single ZnO crystals in ultrapure water was controlled by the density of point defects and screw dislocations on the crystal surface.

Zhang et al.[52] examined surface enthalpies of ZnO crystals possessing different morphologies and consequently demonstrated that nanoparticles and nanoporous composites had significantly lower surface enthalpies than nanorods and nanotetrapods. It was suggested that this arose from the difference in their morphologies, not their sizes. Similar observations were also made by Park et al.[53] in the study on nanocrystalline TiO_2 of different morphologies. In the study of Liu et al.,[54] a correlation between the differences in nanotopography and crystallographic facets present as nanocrystals had a much larger fraction of atoms located at the preferred detachment/dissolution sites.

Mihranyan et al.[55] disputed the classical Ostwald−Freundlich equation, stating that it was inadequate in describing the solubility of highly irregular nanoparticles in their study on dissolution of solid particles with rough surfaces. The surface roughness was modeled as fractal structures, and particles

DOI: 10.1021/acs.langmuir.7b03854
Langmuir 2018, 34, 1645−1654

smaller than 100 nm with the same core diameter but various fractal dimensions exhibited a significant difference in the solubility. Schmidt et al.[56] studied the solubility of TiO_2 nanoparticles within aqueous solutions and observed that material samples containing the amorphous form showed higher solubility than their crystalline counterparts. Avramescu et al.[57] recently investigated the dissolution behavior of Zn, ZnO, and TiO_2 nanomaterials within solutions mimicking body fluids. It was concluded that the crystalline form of TiO_2 was found to be an important factor, as the solubility of nanoanatase was significantly higher than that of nanorutile. In addition, investigated nanomaterials exhibited higher solubility than their bulk counterparts.

Other studies have also supported possible correlations between the solubility of a material and its crystallinity. For example, natural glasses were found to dissolve at least 1.6 orders of magnitude faster compared to their mineral counterparts.[58] Dissolution of hydroxyapatite coatings was associated with its crystallinity.[59] In addition, Li and co-workers[60] found that the solubility of the simultaneously nucleated $Zn(OH)_2$ and ZnO phases in aqueous solution was related to their crystalline nature.

The line profile analysis using the Scherrer equation and the TEM imaging show that the in-house synthesized ZnO nanoparticles were fairly monodisperse, single crystalline. As suggested by the Ostwald–Freundlich equation, their relatively small size and large surface area make them more prone to dissolution, a key initial step in the proposed mechanism by Wu et al.[26] For the larger, polydisperse nanopowder and powder samples, the larger particles consisted of multiple grains with size exceeding that of the in-house synthesized ZnO nanoparticles. The shape anisotropy[19] in the particles might contribute to particle clustering at the drop surface which would suppress the Bénard–Marangoni convections. This is evident from a less pronounced manifestation of the cellular pattern with multiple spokelike radial microstructures of a bow-tie projection compared to the in-house synthesized ZnO nanoparticle sample.

SUMMARY AND CONCLUDING REMARKS

Residual patterns as a result of evaporation induced self-assembly (EISA) from a sessile drop of a reactive nanofluids have not been widely studied previously. As observed by Wu et al.,[26] when a nanofluid droplet containing ZnO nanorods dispersion dries on a substrate, ZnO particles undergo morphological and chemical transformation to form organized structures composed of zinc hydroxide nanofibers. The key step in this process is the initial moisture-assisted dissolution of ZnO nanocrystals, crucial for the formation of soluble $Zn(OH)_2$ complexes. These complexes further assemble into clusters which then form the ultimate polycrystalline residual patterns, with the micromorphology controlled by convective and Marangoni flows and instabilities induced by evaporation of the solvent.

In this work, to shed light on the how different morphologies and crystal structures might impact on proposed dissolution–recrystallization mechanism by Wu et al.,[26] the residual patterns from three different ZnO particles, in-house synthesized ZnO nanoparticles, and commercially acquired (Sigma-Aldrich) ZnO nanopowder and ZnO powder, have been studied. The microscopic and nanoscopic structure of the residual pattern was correlated with that of the starting particles via detailed TEM and XRD analyses. The average coherence length L_a value (from XRD peak broadening analysis) for the in-house prepared ZnO sample was 8.9 ± 0.2 nm compared to those for the ZnO nanopowder and ZnO powder (40.9 ± 1.6 and 44.6 ± 1.8 nm, respectively).

The hierarchical surface patterns generated from evaporation of a 30 μL nanofluid sessile droplet on a silicon substrate showed different morphologies for the three types of ZnO particles used to prepare the nanofluid. For the in-house synthesized ZnO nanoparticles (Figure 4), the substrate was covered by "spokelike" radial structures, similar to those reported for gold nanoparticles on hydrophilic SiO_2/Si substrate.[25] These spokelike radial structures were a solidified manifestation of Bénard–Marangoni cells (Wąsik et al., in preparation) induced by evaporation, and they also resembled the shape of convective cells produced during the evaporation of toluene from polystyrene/toluene solution.[21] Furthermore, a small amount of undissolved ZnO nanoparticle aggregates was found on the constituent fires in only a few areas with a high fiber density (Figure 4h). The residual surface patterns from the nanofluids prepared from the commercially acquired ZnO nanopowder (Figure 5) and powder (Figure 6) appeared as dense layer of spokelike radial patterns covering the entire surface of the silicon substrates. The width (~0.7 μm on average) of the constituent fibers in the residual pattern was similar to that in the in-house synthesized ZnO nanoparticle sample. However, ZnO crystal aggregates were found scattered across the fibrous structures.

Our analyses show that the residual hierarchical surface structures are linked to the morphology, size, and crystallinity of starting ZnO particles through its influence on the initial moisture-assisted rapid dissolution of isobutylamine-coated ZnO nanocrystals. The shape anisotropy of the particles might also play a role in modifying the Marangoni flows and the occurrence of the Bénard–Marangoni instability. Our finding is important to further understanding the novel mechanism underpinning the formation of the complex hierarchical surface patterns from evaporative drying of a reactive nanofluid sessile drop. It also points to the possibility to tailor the structure and morphology of the residual surface patterns for enhanced functionalities from the facile method of evaporative drying of ZnO (and other reactive) nanofluids in nanotechnological applications. A detailed microscopy analysis of the flow dynamics and *in situ* synchrotron X-ray surface scattering in the evaporating droplet would shed further light on the pattern formation mechanism and will be the focus of our future work.

ASSOCIATED CONTENT

Supporting Information

The Supporting Information is available free of charge on the ACS Publications website at DOI: 10.1021/acs.langmuir.7b03854.

SI1: ZnO nanoparticle synthesis; SI2: ZnO particles TEM characterization; SI3: size distribution of ZnO particles; SI4: ZnO particles XRD characterization; SI5: ZnO particles EDX characterization; SI6: DLS of ZnO nano/microfluids; SI7: optical microscopy of the residual surface patterns; SI8: μGIXRD analysis of the residual surface patterns; SI9: coherence length analysis of the residual ZnO nanocrystals in the surface patterns; SI10: Ostwald–Freundlich (modified Kelvin) equation; SI11: aging of ZnO nanofluids (photographs of vials with aged

DOI: 10.1021/acs.langmuir.7b03854
Langmuir 2018, 34, 1645–1654

(nano)fluid solutions left to evaporate in very slow rate) (PDF)

AUTHOR INFORMATION

Corresponding Author

*E-mail wuge.briscoe@bristol.ac.uk; phone +44 (0)117 3318256 (W.H.B.).

ORCID

Wuge H. Briscoe: 0000-0001-8025-960X

Notes

The authors declare no competing financial interest.

ACKNOWLEDGMENTS

Funding from the UK Engineering and Physical Sciences Research Council (EPSRC) through the Bristol Centre for Functional Nanomaterials (BCFN) (grant EP/G036780/1) is acknowledged. H.W. is supported by a Marie Skłodowska-Curie Individual Fellowship (Project Number 656830). W.H.B. acknowledges funding from the EPSRC (EP/H034862/1 and Building Global Engagement in Research (BGER)), European Cooperation in Science and Technology (CMST COST) Action CM1101 "Colloidal Aspects of Nanoscience for Innovative Processes and Materials", and Marie Curie Initial Training Network (MCITN) on "Soft, Small, and Smart: Design, Assembly, and Dynamics of Novel Nanoparticles for Novel Industrial Applications" (NanoS3, Grant no. 290251). Dr. Hazel Sparkes and Dr. Natalie Pridmore are thanked for their help with XRD experiments and Mr. Jonathan Jones and Dr. Sean Davis for their help with TEM and SEM imaging. We thank Dr. Jean-Charles Eloi for the help with EDX analysis and Ms. Anna Slastanova for the help with DLS measurements. We acknowledge the European Synchrotron Radiation Facility for provision of synchrotron radiation facilities (beamline ID13).

REFERENCES

(1) Whitesides, G. M.; Grzybowski, B. Self-Assembly at All Scales. *Science* **2002**, *295* (5564), 2418−2421.

(2) Rodarte, A. L.; Cao, B. H.; Panesar, H.; Pandolfi, R. J.; Quint, M.; Edwards, L.; Ghosh, S.; Hein, J. E.; Hirst, L. S. Self-assembled nanoparticle micro-shells templated by liquid crystal sorting. *Soft Matter* **2015**, *11* (9), 1701−1707.

(3) Han, W.; Lin, Z. Learning from "Coffee Rings": Ordered Structures Enabled by Controlled Evaporative Self-Assembly. *Angew. Chem., Int. Ed.* **2012**, *51* (7), 1534−1546.

(4) Pilkington, G. A.; Briscoe, W. H. Nanofluids mediating surface forces. *Adv. Colloid Interface Sci.* **2012**, *179-182*, 68−84.

(5) Briscoe, W. H. Depletion forces between particles immersed in nanofluids. *Curr. Opin. Colloid Interface Sci.* **2015**, *20* (1), 46−53.

(6) Dinh, N. T.; Sowade, E.; Blaudeck, T.; Hermann, S.; Rodriguez, R. D.; Zahn, D. R. T.; Schulz, S. E.; Baumann, R. R.; Kanoun, O. High-resolution inkjet printing of conductive carbon nanotube twin lines utilizing evaporation-driven self-assembly. *Carbon* **2016**, *96*, 382−393.

(7) Janowska, I. Evaporation-induced self-assembling of few-layer graphene into a fractal-like conductive macro-network with a reduction of percolation threshold. *Phys. Chem. Chem. Phys.* **2015**, *17* (12), 7634−7638.

(8) Shim, J.; Yun, J. M.; Yun, T.; Kim, P.; Lee, K. E.; Lee, W. J.; Ryoo, R.; Pine, D. J.; Yi, G.-R.; Kim, S. O. Two-Minute Assembly of Pristine Large-Area Graphene Based Films. *Nano Lett.* **2014**, *14* (3), 1388−1393.

(9) Dugas, V.; Broutin, J.; Souteyrand, E. Droplet Evaporation Study Applied to DNA Chip Manufacturing. *Langmuir* **2005**, *21* (20), 9130−9136.

(10) Cheng, W.; Niederberger, M. Evaporation-Induced Self-Assembly of Ultrathin Tungsten Oxide Nanowires over a Large Scale for Ultraviolet Photodetector. *Langmuir* **2016**, *32* (10), 2474−2481.

(11) Mitome, T.; Hirota, Y.; Uchida, Y.; Nishiyama, N. Porous structure and pore size control of mesoporous carbons using a combination of a soft-templating method and a solvent evaporation technique. *Colloids Surf., A* **2016**, *494*, 180−185.

(12) Uchiyama, H.; Sasaki, R.; Kozuka, H. Evaporation-driven self-organization of photoluminescent organic dye-doped silica-poly-(vinylpyrrolidone) hybrid films prepared by low-speed dip-coating. *Colloids Surf., A* **2014**, *453*, 1−6.

(13) Thokchom, A. K.; Swaminathan, R.; Singh, A. Fluid Flow and Particle Dynamics Inside an Evaporating Droplet Containing Live Bacteria Displaying Chemotaxis. *Langmuir* **2014**, *30* (41), 12144−12153.

(14) Mahmud, M. A.; MacDonald, B. D. Experimental investigation of interfacial energy transport in an evaporating sessile droplet for evaporative cooling applications. *Phys. Rev. E: Stat. Phys., Plasmas, Fluids, Relat. Interdiscip. Top.* **2017**, *95*, 012609.

(15) Deegan, R. D. Pattern formation in drying drops. *Phys. Rev. E: Stat. Phys., Plasmas, Fluids, Relat. Interdiscip. Top.* **2000**, *61* (1), 475−485.

(16) Deegan, R. D.; Bakajin, O.; Dupont, T. F.; Huber, G.; Nagel, S. R.; Witten, T. A. Capillary flow as the cause of ring stains from dried liquid drops. *Nature* **1997**, *389* (6653), 827−829.

(17) Deegan, R. D.; Bakajin, O.; Dupont, T. F.; Huber, G.; Nagel, S. R.; Witten, T. A. Contact line deposits in an evaporating drop. *Phys. Rev. E: Stat. Phys., Plasmas, Fluids, Relat. Interdiscip. Top.* **2000**, *62* (1), 756−765.

(18) Hu, H.; Larson, R. G. Marangoni Effect Reverses Coffee-Ring Depositions. *J. Phys. Chem. B* **2006**, *110* (14), 7090−7094.

(19) Yunker, P. J.; Still, T.; Lohr, M. A.; Yodh, A. G. Suppression of the coffee-ring effect by shape-dependent capillary interactions. *Nature* **2011**, *476* (7360), 308−311.

(20) Getling, A. V.; Brausch, O. Cellular flow patterns and their evolutionary scenarios in three-dimensional Rayleigh-B\'enard convection. *Phys. Rev. E: Stat. Phys., Plasmas, Fluids, Relat. Interdiscip. Top.* **2003**, *67* (4), 046313.

(21) Bassou, N.; Rharbi, Y. Role of Bénard−Marangoni Instabilities during Solvent Evaporation in Polymer Surface Corrugations. *Langmuir* **2009**, *25* (1), 624−632.

(22) Pauliac-Vaujour, E.; Stannard, A.; Martin, C. P.; Blunt, M. O.; Notingher, I.; Moriarty, P. J.; Vancea, I.; Thiele, U. Fingering Instabilities in Dewetting Nanofluids. *Phys. Rev. Lett.* **2008**, *100* (17), 176102.

(23) Homsy, G. M. Viscous fingering in porous media. *Annu. Rev. Fluid Mech.* **1987**, *19*, 271−311.

(24) Ajaev, V. S. Evolution of dry patches in evaporating liquid films. *PhRvE* **2005**, *72* (3), 031605.

(25) Huang, J.; Kim, F.; Tao, A. R.; Connor, S.; Yang, P. Spontaneous formation of nanoparticle stripe patterns through dewetting. *Nat. Mater.* **2005**, *4* (12), 896−900.

(26) Wu, H.; Chen, L. X.; Zeng, X. Q.; Ren, T. H.; Briscoe, W. H. Self-assembly in an evaporating nanofluid droplet: rapid transformation of nanorods into 3D fibre network structures. *Soft Matter* **2014**, *10* (29), 5243−5248.

(27) Sun, B.; Sirringhaus, H. Solution-Processed Zinc Oxide Field-Effect Transistors Based on Self-Assembly of Colloidal Nanorods. *Nano Lett.* **2005**, *5* (12), 2408−2413.

(28) Dane, T. G. pyGIX; https://github.com/tgdane/pygix.

(29) Ashiotis, G.; Deschildre, A.; Nawaz, Z.; Wright, J. P.; Karkoulis, D.; Picca, F. E.; Kieffer, J. The fast azimuthal integration Python library: pyFAI. *J. Appl. Crystallogr.* **2015**, *48* (2), 510−519.

(30) Scherrer, P. Estimation of the size and internal structure of colloidal particles by means of röntgen. *Nachr. Ges. Wiss. Göttingen* **1918**, *2*, 96−100.

(31) Dane, T. G.; Bartenstein, J. E.; Sironi, B.; Mills, B. M.; Alexander Bell, O.; Emyr Macdonald, J.; Arnold, T.; Faul, C. F. J.; Briscoe, W. H.

DOI: 10.1021/acs.langmuir.7b03854
Langmuir 2018, 34, 1645−1654

Influence of solvent polarity on the structure of drop-cast electroactive tetra(aniline)-surfactant thin films. *Phys. Chem. Chem. Phys.* **2016**, *18* (35), 24498−24505.
(32) Sironi, B.; Snow, T.; Redeker, C.; Slastanova, A.; Bikondoa, O.; Arnold, T.; Klein, J.; Briscoe, W. H. Structure of lipid multilayers via drop casting of aqueous liposome dispersions. *Soft Matter* **2016**, *12* (17), 3877−3887.
(33) Bragg, W. H.; Bragg, W. L. The Reflection of X-rays by Crystals. *Proc. R. Soc. London, Ser. A* **1913**, *88* (605), 428−438.
(34) Williamson, G. K.; Hall, W. H. X-ray line broadening from filed aluminium and wolfram. *Acta Metall.* **1953**, *1* (1), 22−31.
(35) Langford, J. I.; Wilson, A. J. C. Scherrer after sixty years: A survey and some new results in the determination of crystallite size. *J. Appl. Crystallogr.* **1978**, *11* (2), 102−113.
(36) Leoni, M.; Di Maggio, R.; Polizzi, S.; Scardi, P. X-ray Diffraction Methodology for the Microstructural Analysis of Nanocrystalline Powders: Application to Cerium Oxide. *J. Am. Ceram. Soc.* **2004**, *87* (6), 1133−1140.
(37) Zender, C. Particle size distributions: theory and application to aerosols, clouds, and soils, 2013; http://dust.ess.uci.edu/facts/psd/psd.pdf (accessed on 12th Dec 2017).
(38) Pacholski, C.; Kornowski, A.; Weller, H. Self-Assembly of ZnO: From Nanodots to Nanorods. *Angew. Chem., Int. Ed.* **2002**, *41* (7), 1188−1191.
(39) Xu, S.; Wang, Z. One-dimensional ZnO nanostructures: Solution growth and functional properties. *Nano Res.* **2011**, *4* (11), 1013−1098.
(40) Jiang, H. G.; Rühle, M.; Lavernia, E. J. On the applicability of the x-ray diffraction line profile analysis in extracting grain size and microstrain in nanocrystalline materials. *J. Mater. Res.* **1999**, *14* (02), 549−559.
(41) van der Walt, S.; Colbert, S. C.; Varoquaux, G. The NumPy Array: A Structure for Efficient Numerical Computation. *Comput. Sci. Eng.* **2011**, *13* (2), 22−30.
(42) Song, B.; Cui, X.; Wang, Y.; Si, L.; Kou, Z.; Tian, W.; Yi, C.; Sun, Y. Controllable Growth of Unique Three-Dimensional Layered Basic Zinc Salt/ZnO Binary Structure. *Cryst. Growth Des.* **2016**, *16* (9), 4877−4885.
(43) Song, R. Q.; Xu, A. W.; Deng, B.; Li, Q.; Chen, G. Y. From Layered Basic Zinc Acetate Nanobelts to Hierarchical Zinc Oxide Nanostructures and Porous Zinc Oxide Nanobelts. *Adv. Funct. Mater.* **2007**, *17* (2), 296−306.
(44) Poul, L.; Jouini, N.; Fiévet, F. Layered Hydroxide Metal Acetates (Metal = Zinc, Cobalt, and Nickel): Elaboration via Hydrolysis in Polyol Medium and Comparative Study. *Chem. Mater.* **2000**, *12* (10), 3123−3132.
(45) Song, B.; Wang, Y.; Cui, X.; Kou, Z.; Si, L.; Tian, W.; Yi, C.; Wei, T.; Sun, Y. A Series of Unique Architecture Building of Layered Zinc Hydroxides: Self-Assembling Stepwise Growth of Layered Zinc Hydroxide Carbonate and Conversion into Three-Dimensional ZnO. *Cryst. Growth Des.* **2016**, *16* (2), 887−894.
(46) Kaptay, G. On the size and shape dependence of the solubility of nano-particles in solutions. *Int. J. Pharm.* **2012**, *430* (1−2), 253−257.
(47) David, C. A.; Galceran, J.; Rey-Castro, C.; Puy, J.; Companys, E.; Salvador, J.; Monné, J.; Wallace, R.; Vakourov, A. Dissolution Kinetics and Solubility of ZnO Nanoparticles Followed by AGNES. *J. Phys. Chem. C* **2012**, *116* (21), 11758−11767.
(48) Mudunkotuwa, I. A.; Rupasinghe, T.; Wu, C.-M.; Grassian, V. H. Dissolution of ZnO Nanoparticles at Circumneutral pH: A Study of Size Effects in the Presence and Absence of Citric Acid. *Langmuir* **2012**, *28* (1), 396−403.
(49) Meulenkamp, E. A. Size Dependence of the Dissolution of ZnO Nanoparticles. *J. Phys. Chem. B* **1998**, *102* (40), 7764−7769.
(50) Gerischer, H.; Sorg, N. Chemical dissolution of zinc oxide crystals in aqueous electrolytes—An analysis of the kinetics. *Electrochim. Acta* **1992**, *37* (5), 827−835.
(51) Michaelis, M.; Fischer, C.; Colombi Ciacchi, L.; Luttge, A. Variability of Zinc Oxide Dissolution Rates. *Environ. Sci. Technol.* **2017**, *51* (8), 4297−4305.
(52) Zhang, P.; Xu, F.; Navrotsky, A.; Lee, J. S.; Kim, S.; Liu, J. Surface Enthalpies of Nanophase ZnO with Different Morphologies. *Chem. Mater.* **2007**, *19* (23), 5687−5693.
(53) Park, T.-J.; Levchenko, A. A.; Zhou, H.; Wong, S. S.; Navrotsky, A. Shape-dependent surface energetics of nanocrystalline TiO_2. *J. Mater. Chem.* **2010**, *20* (39), 8639−8645.
(54) Liu, J.; Aruguete, D. M.; Murayama, M.; Hochella, M. F. Influence of Size and Aggregation on the Reactivity of an Environmentally and Industrially Relevant Nanomaterial (PbS). *Environ. Sci. Technol.* **2009**, *43* (21), 8178−8183.
(55) Mihranyan, A.; Strømme, M. Solubility of fractal nanoparticles. *Surf. Sci.* **2007**, *601* (2), 315−319.
(56) Schmidt, J.; Vogelsberger, W. Aqueous Long-Term Solubility of Titania Nanoparticles and Titanium(IV) Hydrolysis in a Sodium Chloride System Studied by Adsorptive Stripping Voltammetry. *J. Solution Chem.* **2009**, *38* (10), 1267−1282.
(57) Avramescu, M.-L.; Rasmussen, P. E.; Chénier, M.; Gardner, H. D. Influence of pH, particle size and crystal form on dissolution behaviour of engineered nanomaterials. *Environ. Sci. Pollut. Res.* **2017**, *24* (2), 1553−1564.
(58) Wolff-Boenisch, D.; Gislason, S. R.; Oelkers, E. H. The effect of crystallinity on dissolution rates and CO_2 consumption capacity of silicates. *Geochim. Cosmochim. Acta* **2006**, *70* (4), 858−870.
(59) Xue, W.; Liu, X.; Zheng, X.; Ding, C. Effect of hydroxyapatite coating crystallinity on dissolution and osseointegration in vivo. *J. Biomed. Mater. Res., Part A* **2005**, *74A* (4), 553−561.
(60) Li, P.; Liu, H.; Lu, B.; Wei, Y. Formation Mechanism of 1D ZnO Nanowhiskers in Aqueous Solution. *J. Phys. Chem. C* **2010**, *114* (49), 21132−21137.

DOI: 10.1021/acs.langmuir.7b03854
Langmuir 2018, 34, 1645−1654